
This is an electronic reprint of the original article.
This reprint may differ from the original in pagination and typographic detail.

Mousapour, Mehrdad; Kumar, S. Siddharth; Partanen, Jouni; Salmi, Mika

3d printing of a continuous carbon fiber reinforced bronze-matrix composite using material extrusion

Published in:
Composites Part B: Engineering

DOI:
[10.1016/j.compositesb.2024.111961](https://doi.org/10.1016/j.compositesb.2024.111961)

Published: 15/01/2025

Document Version
Publisher's PDF, also known as Version of record

Published under the following license:
CC BY

Please cite the original version:
Mousapour, M., Kumar, S. S., Partanen, J., & Salmi, M. (2025). 3d printing of a continuous carbon fiber reinforced bronze-matrix composite using material extrusion. *Composites Part B: Engineering*, 289, Article 111961. <https://doi.org/10.1016/j.compositesb.2024.111961>

This material is protected by copyright and other intellectual property rights, and duplication or sale of all or part of any of the repository collections is not permitted, except that material may be duplicated by you for your research use or educational purposes in electronic or print form. You must obtain permission for any other use. Electronic or print copies may not be offered, whether for sale or otherwise to anyone who is not an authorised user.



3d printing of a continuous carbon fiber reinforced bronze-matrix composite using material extrusion

Mehrdad Mousapour^{*}, S Siddharth Kumar, Jouni Partanen, Mika Salmi

Department of Mechanical Engineering, Aalto University, Puumiehenkuja 3, 02150, Espoo, Finland

ARTICLE INFO

Handling Editor: Prof. Ole Thomsen

Keywords:

Additive manufacturing (AM)
Continuous carbon fiber (CCF)
Material extrusion (MEX)
Copper base alloy

ABSTRACT

The main objective of this study is to investigate, for the first time, the feasibility of 3d printing a continuous carbon fiber (CCF) reinforced metal matrix composite using a cost-effective material extrusion (MEX) technology. Notably, this paper presents a detailed analysis of the microstructure and mechanical and physical properties of a bronze matrix composite reinforced with CCF. The results reveal that CCF significantly impedes the expected densification levels of the composite's structure, causing extensive gaps between the bronze particles. However, despite the high porosity level, the composite's electrical conductivity remains relatively high, demonstrating the limited negative impact of the CCF material on the composite's conductivity. Moreover, mechanical evaluations were performed through 3-point bending and tensile tests, highlighting the composite material's advantages and limitations. The results show that the composite material exhibits an improved yield stress of 76 %, increased ultimate tensile strength of 20 %, and an extended fracture strain of 30 %. However, the flexural strength decreases by 23 % due to the presence of massive gaps formed by CCF.

1. Introduction

Continuous carbon fiber (CCF) is a notable high-strength reinforcement utilized in the composition of lightweight and strong composite materials due to its superior properties, such as high strength, stiffness, durability, and design flexibility [1–6]. CCF comprises long, thin carbon fiber strands bundled into integrated tows to create composite components. The composite components use a resin such as epoxy or vinyl ester, which binds and transfers load between the fibers, resulting in a material with superior properties than the individual components [7]. Owing to its excellent features, CCF is becoming increasingly popular in various industries such as aerospace [8], automotive [9,10], civil engineering [11,12], and sporting goods [13,14], making it a critical component in the development of modern-day advanced materials.

Recently, the implementation of 3D printing technology has facilitated the development of intricate structures previously deemed challenging or unachievable through traditional manufacturing methods [15–20]. One of the significant aspects of this technology is its potential to produce composite materials with impeccable precision, especially those reinforced with CCF [21–24]. The benefits of 3D printing technology in fabricating CCF-reinforced composite materials are vast and diverse, including cost-effectiveness, production of parts with complex

geometries, and the ability to print intricate designs. With the application of 3D printing technology in producing CCF-reinforced composite materials, there is significant promise for creating high-performance materials with tailored properties that meet specific needs [25–28]. Despite the significant advancements in 3D printing technology, the successful manufacturing of CCF composite material is still a complicated process, which requires consideration of several factors that include but are not limited to fiber orientation, curing, and printing parameters that affect the overall quality and mechanical properties of the material [29,30].

Various studies have investigated using different additive manufacturing techniques to fabricate continuous carbon fiber-reinforced polymer (CFRP) components. Heidari et al. [31] conducted mechanical tests to analyze the influence of different printing parameters on the strength and modulus of material extrusion (MEX) 3D printed carbon fiber-reinforced PLA composites. They identified the optimal printing conditions for enhancing their mechanical performance. Furthermore, Lu et al. [32] utilized a novel technique for fabricating CCFRP composites using vat photopolymerization (CONFIB-VPP) and demonstrated the feasibility and advantages of this approach through experiments and finite element analysis. In another work, Kumar et al. [33] demonstrated the feasibility of using CCF reinforcement in

^{*} Corresponding author.

E-mail address: mehrdad.mousapour@aalto.fi (M. Mousapour).

<https://doi.org/10.1016/j.compositesb.2024.111961>

Received 28 May 2024; Received in revised form 22 October 2024; Accepted 6 November 2024

Available online 7 November 2024

1359-8368/© 2024 The Authors. Published by Elsevier Ltd. This is an open access article under the CC BY license (<http://creativecommons.org/licenses/by/4.0/>).

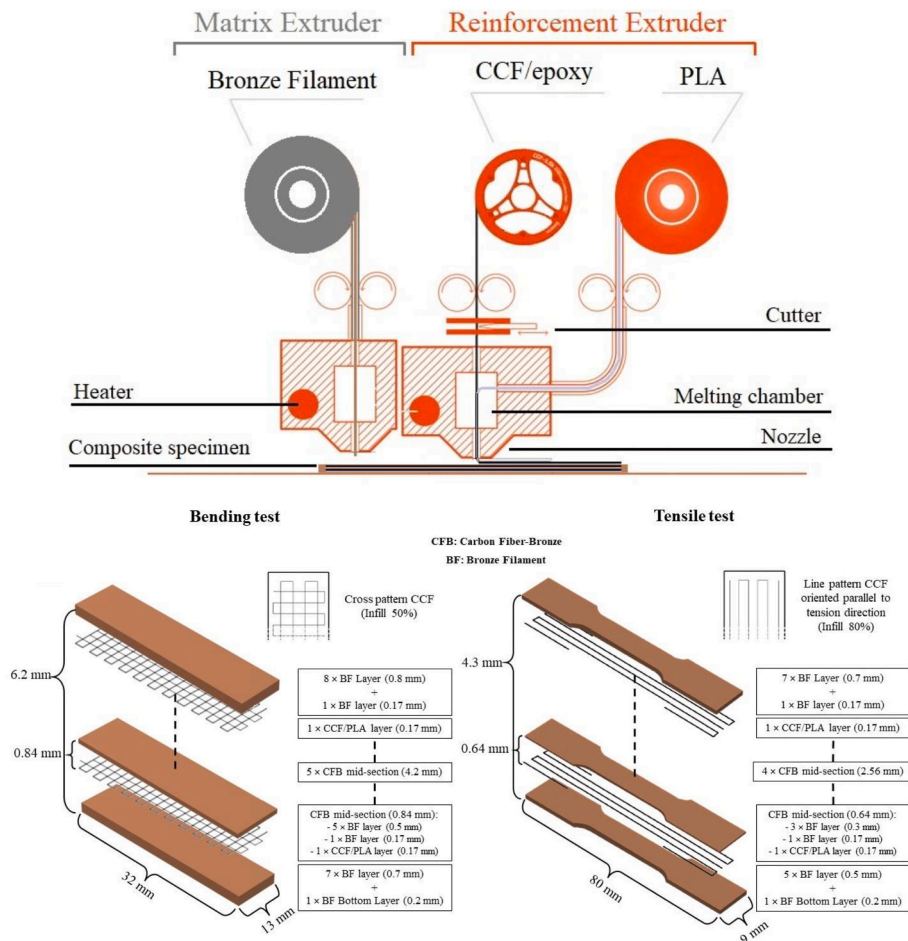


Fig. 1. Schematics depicting the nozzles for printing CCFR-bronze composite, and the bending and tensile test specimens with the layer structure design.

conjunction with shape memory polymer to produce programmable, stimuli-responsive structures through 4D printing technology. Akmal et al. [34] demonstrated 3D printing self-sensing capabilities of CCF and metal wires in a plastic matrix. Their research evaluated the mechanical properties of these structures under different temperatures and moistures. Additionally, new numerical methods and modelling can be helpful to analyze the mechanical properties of composite materials [35]. On the other side, additive manufacturing techniques have yet to be widely utilized in the fabrication of components made of continuous carbon fiber-reinforced metals (CFRMs), with conventional methods being the predominant manufacturing approach adopted in this field. In CFRMs, the fabrication procedures are usually divided into three primary categories: (a) solid-state processing, (b) liquid-state processing, and (c) deposition processing [36]. Powder metallurgy and casting are widely employed conventional techniques for enhancing the mechanical properties of CFRMs. The addition of carbon fiber to different composites leads to an increase in hardness and ultimate tensile strength. Some composites also demonstrate significant enhancements in both tensile and compressive properties. These techniques utilize a variety of metal matrices, such as aluminum [37–41], magnesium [42], copper [43–46], and titanium [47–49]. The present state of research indicates an apparent gap in knowledge regarding the additive manufacturing of CFRMs. Further investigations are required to expand our understanding of this domain for the development of innovative and efficient manufacturing techniques.

Cu10Sn alloy has become a promising material for electronic packaging, bearings, and other industrial applications, with its excellent electrical conductivity, good machinability, and high corrosion resistance [50–53]. The porous bronze is a high-performance candidate for

energy conversion and storage, catalysis, and filtration applications. Additionally, Cu10Sn porous materials that can create a lubricating film in the presence of moisture are self-lubricating and have gained popularity as a potential material choice for sliding components such as bearings and bushings [54–56]. On the other side, 3D printing of Cu10Sn allows for the production of complex structures and customized parts with precise dimensions, which can be used in manufacturing and engineering applications [57,58]. This study explores the feasibility of producing a CCF-reinforced bronze matrix composite by utilizing an affordable 3d printing technology, particularly MEX. Furthermore, this investigation evaluates the mechanical and physical properties of the sintered composite, which will be compared to those of the sintered bronze part. This comparative analysis can give a deeper understanding of the effectiveness of incorporating CCF into a bronze matrix. The results of this study may contribute to the development of intricate and mechanically enhanced porous bronze structures, which could present challenges for production using conventional methods. These structures have potential applications in aerospace, marine, and automotive industries, serving as bearings (attributed to self-lubricating properties and enhanced mechanical attributes), bushings, as well as electrical contacts, connectors, and switches (owing to their high electrical conductivity).

2. Material and methods

2.1. Materials and equipment

In this study, Cu10Sn Bronze Filament™ (The Virtual Foundry, USA; Copper: 89.80 %, Tin: 10.20 %) and CCF filament (Anisoprint Sarl,

Table 1
Printing parameters used for CCFR-bronze specimens.

Parameters	Values
Macro-layer height (CCF layer) (mm)	0.17
Bottom layer height (mm)	0.2
Bronze layer height (mm)	0.1
Bronze shell layer height (mm)	0.17
Matrix (bronze filament) flow rate (%)	150
CCF infill density for bending test specimen (%) / pattern	50 / cross
CCF infill density for tensile test specimen (%) / pattern	80 / line
Matrix (bronze filament) extruder temperature (°C)	265
CCF-PLA extruder temperature (°C)	215
Build plate temperature (°C)	60
Printing speed (mm/s)	50
Matrix (bronze filament) / CCF-PLA extruder nozzle diameter (mm)	0.6 / 0.25

Luxembourg) were used to produce a continuous carbon fiber-reinforced bronze composite (CCFR-bronze). The Bronze Filament with a diameter of 1.75 mm and a density of 4.5 g/cm³ contains PLA as the binder and a metal content of 89 wt-%. According to the manufacturer, the d70 particle size for bronze powder is 44 μm. The CCF filament utilized in this study consists of 1.5 K carbon fiber, exhibiting a tensile strength of 2200 MPa and an elastic modulus of 149 ± 5 GPa. The filament has a diameter of 0.35 mm and incorporates a 60 % carbon fiber volume fraction (from Anisoprint company). The specific production process of this filament is documented in references [59,60]. The filament is impregnated with a specialized combination of photopolymer and epoxy, which serves as the thermoset matrix for the filament tow due to optimizing its printability and also mechanical, thermal, and chemical properties. For this study, an Anisoprint Composer A4 3d printer (Anisoprint Sarl, Luxembourg) was used to generate the specimens due to its composite fiber co-extrusion technology, which makes it possible to impregnate the carbon fiber optimally into the matrix. Following the printer's mechanism, a co-extruder material (plastic) is simultaneously extruded with the CCF/epoxy filament, effectively securing the CCF in place during the printing process. Fig. 1 presents a schematic of both extruders utilized in this printer.

2.2. Specimen preparation

Standard test specimens of bronze and CCFR-bronze for bending (ASTM standard B 528-99: 32 × 13 × 6.2 ± 0.05 mm) and tensile (ASTM standard E 8: 80 × 9 × 4.3 ± 0.05 mm) tests were designed using SolidWorks (Dassault Systèmes SOLIDWORKS Corp., Waltham, USA). The STL files were imported into Aura software (Version 1.27.2, Anisoprint Sarl, Luxembourg) to generate the G-code. Custom layers were created to precisely control the amount of carbon fiber printed, minimize large air voids, and ensure maximum carbon fiber adhesion with the matrix (bronze) in the composite specimens. By default, the Aura algorithm generates G-code that deposits carbon fiber alongside the co-extruded material (PLA) in every internal layer, lacking the ability to selectively determine which layers receive carbon fiber. Additionally, it fails to infill the interior region with bronze (matrix) material, resulting in substantial air gaps that diminish composite integrity and impede the effectiveness of fiber-to-bronze adhesion. To address this, multiple G-codes were generated using different layer settings and flow rates in Aura. Subsequently, the layers were extracted and generalized for placement as needed. Finally, the layers were carefully combined by adjusting the G-code parameters (Fig. 1) using MATLAB (R2022a, MathWorks, Natick, USA). This methodology facilitated the generation of G-code files with precise layer configurations customized to the individual specimen design, incorporating pure matrix layers to eliminate large air gaps and enabling the utilization of different layer heights. The manipulation of layer heights allowed for optimization of the carbon fiber layers, while smaller layer heights in the pure matrix layers maximized resolution. In the bending and tensile composite specimens, the CCF filament was printed in cross and parallel line patterns,

respectively. The key parameters used for printing both bronze and CCFR-bronze specimens are outlined in Table 1. These parameters were chosen based on the material data sheet recommendations and the default printing settings. Due to the high metal content of the bronze filament, a temperature of 265 °C was selected to facilitate a smoother flow of extrusion of the material. The next bronze layer directly above the printed CCF layer, referred to as the bronze shell layer, was chosen to have equal thickness to that of the CCF layer (0.17 mm) to prevent wearing away the printed CCF. Additionally, the flow rate of the bronze (matrix) was set at 150 % to ensure coverage of the spaces between the CCF lines and to minimize gaps in the printed structure. Two distinct patterns were employed for printing the CCF in preparation for bending and tensile testing. A cross pattern, featuring 50 % infill, was utilized for bending tests, while a line pattern oriented parallel to the direction of tension, with 80 % infill, was chosen for the production of tensile test specimens. The infill percentage is a specific value determined by Aura software, depending on the pattern type, and should not be conflated with the volume fraction of the printed CCF filament. The volume fractions of bronze and CCF filaments utilized for the bending and tensile specimens (0.9/0.1 and 0.94/0.06, respectively) were determined based on data from the Aura software, filament density values provided by the manufacturers, and microstructural observations from the cross section. The selection of the patterns and infill percentages was based on empirical experimentation conducted during this and previous research [33]. The objective was to establish optimal printing parameters that minimize voids within the matrix and enhance the orientation of continuous carbon fiber (CCF) for improved effectiveness.

The printed specimens were placed in an alumina container and covered entirely with Al₂O₃, CaO, and SiO₂ powder ballast. The purpose of the ballast powder was to protect the specimens from oxidation. This container was then inserted into a horizontal tube furnace (Nanoe, Zsinter 2-5-17TPD2, France) for debinding (removal of the binding agent from the printing process) and sintering processes. A B-type thermocouple was connected to a logger outside the furnace to record the temperature. According to the manufacturer's recommendations, the debinding process was done in two stages: firstly, the temperature was increased at 2 K/min from room temperature up to 300 °C (with no held), and secondly, the temperature was raised at 1 K/min up to 450 °C and held for 1 h. The sintering process started immediately following the de-binding process, while the position of the specimen remained unchanged. The temperature was raised by 3 K/min until reaching the target sintering temperature of 900 °C, where it was held for a duration of 5 h. Lastly, the specimens were cooled down at a 3 K/min rate. The entire debinding, sintering, and cooling processes were conducted in an argon atmosphere with a flow rate of 0.5 l/min.

2.3. Materials characterization and testing procedures

After sintering, the density of the specimens was measured using the Archimedes principle as described in DIN ISO 3369. That was performed to assess the densification parameter (ψ) and porosity, which is mathematically represented as [61]:

$$\Psi = ((\rho_{\text{sinter}} - \rho_{\text{brown}}) / (\rho_{\text{th}} - \rho_{\text{brown}})) \quad (1)$$

$$\text{Porosity (\%)} = [1 - (\rho_{\text{sinter}} / \rho_{\text{th}})] \times 100 \quad (2)$$

Here, ρ_{sinter} denotes the sintered density (g/cm³), ρ_{brown} represents the density of debound parts (g/cm³), and ρ_{th} is the theoretical density (g/cm³). The theoretical and apparent densities of Cu10Sn were determined to be 8.76 and 4.69 g/cm³, respectively. Additionally, a digital caliper measured the dimensional changes and shrinkage rate of the specimens after sintering. The electrical conductivity was determined using a conductivity meter (Ossila Limited, UK) based on the four-point probe method, which involves passing a current through two outer electrodes and measuring the voltage across two inner electrodes. The electrical conductivity was measured from three different areas,

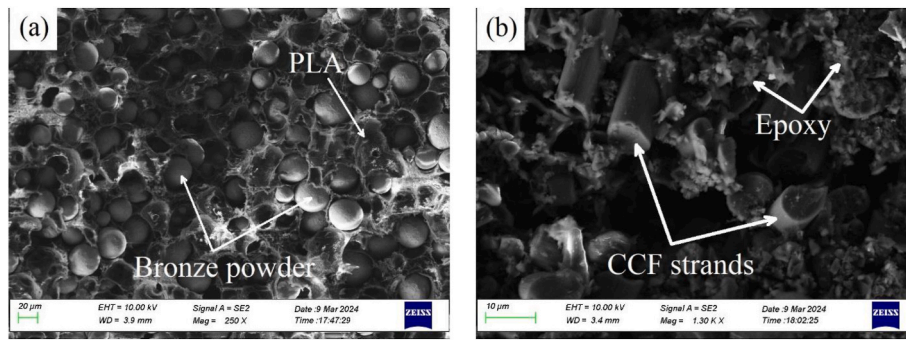


Fig. 2. SEM image from a cross-section of (a) Bronze Filamet™ and (b) CCF filament.

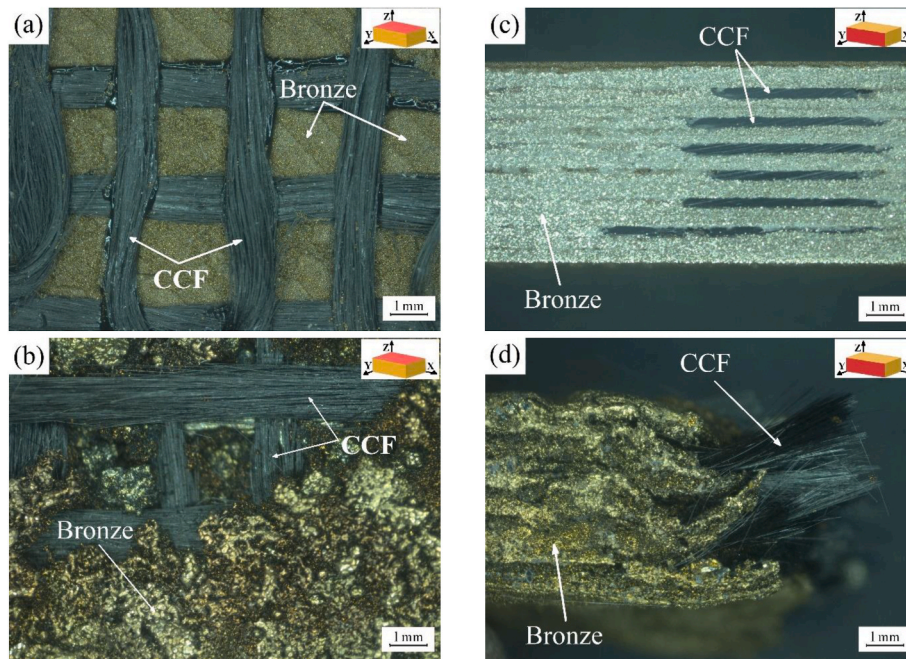


Fig. 3. The macrostructure images of the CCFR-bronze from the top view: (a) the printed and (b) sintered specimens; and side view: (c) printed and (d) sintered specimens.

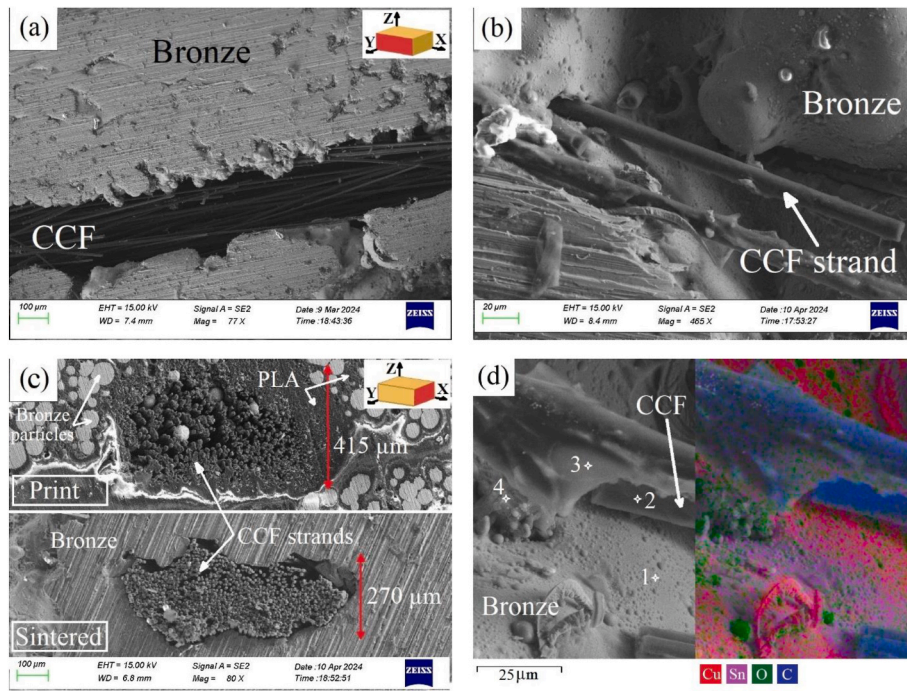
including the top and bottom surfaces as well as the cross-section (center) of each specimen. The microstructure of the specimens was examined with an optical microscope (Zeiss Stemi 508, Germany), and the bonding between Cu10Sn and CCF, as well as the elemental distribution, were evaluated using a scanning electron microscope (SEM; Zeiss Sigma VP, Germany) equipped with an energy-dispersive spectrometer (EDS; Oxford Ultimmax, UK). Furthermore, to compare the mechanical properties of the composite with the bronze specimen (without CCF), both the 3-point bending test (ASTM standard B 528-99) and the tensile test (ASTM standard E 8) were performed using a universal testing machine (MTS insight, USA). The span length chosen for the bending test was 24.5 mm, and the rates used for the bending and tensile tests were 0.03 mm/s and 0.01 mm/s, respectively. All the tests were conducted at least three times to guarantee the reliability of data.

3. Results and discussion

The SEM images from the cross-section of both bronze and CCF filaments are presented in Fig. 2, which illustrates spherical shape bronze particles and carbon fiber strands in the binders. The macrostructure of the CCFR-bronze specimen is analyzed from top and side views and shown in Fig. 3. For better observation of the printed CCF within bronze

particles, a thin layer of bronze from the top of the CCFR-bronze specimen is partially removed before and after sintering. The CCF strands keep their shape (cross pattern) after sintering while surrounded by sintered bronze particles (Fig. 3b). Fig. 3c indicates a side view of the CCFR-bronze print; the side surface is polished to make the CCF (black lines) visible. A side view of the sintered CCFR-bronze after the bending test is also shown in Fig. 3d, in which the bronze matrix is deformed and eventually ruptured. However, in macro-observation, CCF remains in a good connection with the matrix.

The microstructure of the CCFR-bronze is depicted in Fig. 4 to study the connection between the composite components in more detail. As evidenced by the SEM image taken from the composite's polished surface (side-view), CCF strands create massive disconnections (gaps) in the matrix structure so that the bronze particles cannot fill the spaces between strands. At the interface area, however, the CCF strands have sufficient cohesion with bronze particles, represented by higher magnification in Fig. 4b. Moreover, the microstructure from the cross-section of the CCFR-bronze before and after sintering, indicated in Fig. 4c, provides a better view of CCF strands within the bronze structure. This microstructure shows that the distance between the strands is diminished (from 415 μm to 270 μm) in the z direction after sintering, probably due to gravitational force. Similar results have been observed



Elements	Cu	Sn	C	O
Point	(wt-%)	(wt-%)	(wt-%)	(wt-%)
1	63.94	9.74	24.28	2.04
2	3.41	-	87.35	9.24
3	8.38	0.91	81.72	8.99
4	59.28	6.97	31.24	2.51

Fig. 4. The microstructure of CCFR-bronze from a) the side view, b) the interface area between bronze and CCF strands, and c) the cross-section before and after sintering. d) Mapping and EDS point analysis from the interface area.

Table 2
The density values and shrinkage rate of bronze and CCFR-bronze specimens.

Specimen	Printed density (g/cm ³)	Debound density (g/cm ³)	Sintered density (g/cm ³)	Densification parameter (%)	Sintering shrinkage (%)		
					x	y	z
Bronze	4.65	4.50	6.36	43.8	13.77	13.36	14.01
CCFR-bronze	3.96	3.88	4.45	11.6	6.71	7.76	8.9

in other studies [62–65], demonstrating the effect of gravitational force on the rearrangement of metal particles and the sintering process. In fact, after sintering, the CCF strands become denser at the core, while bronze particles fill the spaces between the interface strands. However, the considerable magnitude of the gap remains (Fig. 4a) and has

noticeable effects on the mechanical properties of the CCFR-bronze.

Further explanation of these effects will be provided in subsequent sections of this manuscript. To better understand the elemental distribution in the CCFR-bronze microstructure, the EDS mapping and point analysis are examined from the interface area between the CCF strands

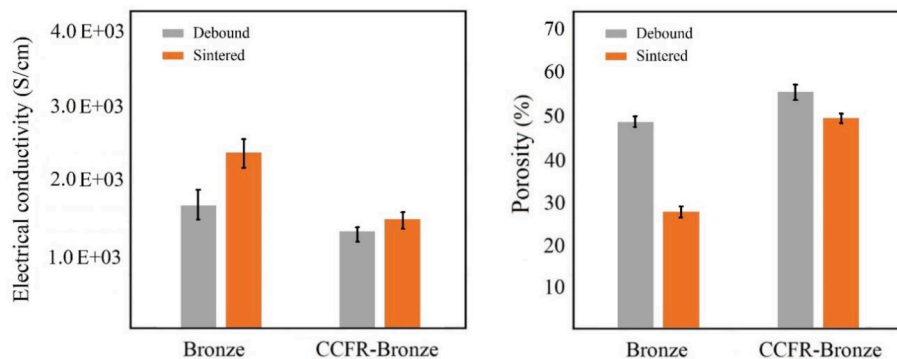


Fig. 5. The average of measured electrical conductivity and porosity of both bronze and CCFR-bronze before and after sintering at room temperature.

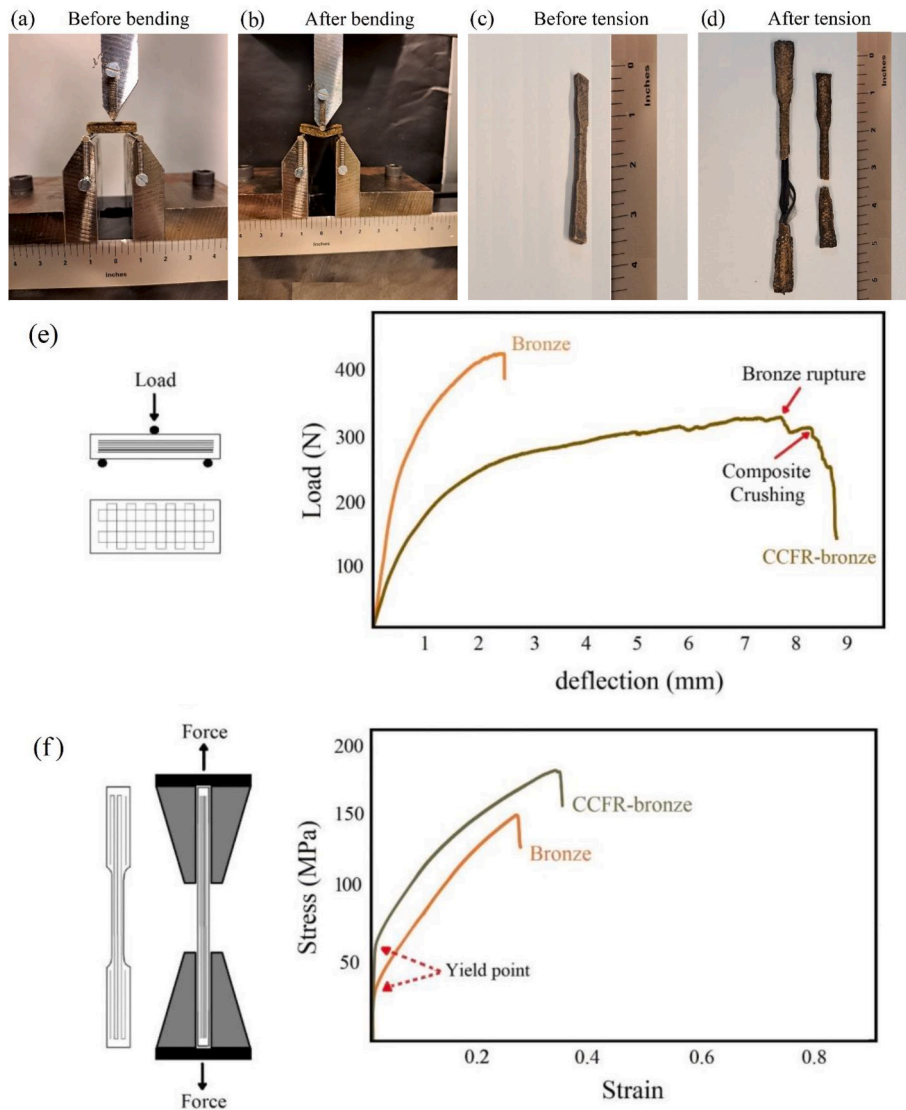


Fig. 6. Images of bronze and CCFR-bronze specimens before and after bending (a,b) and tensile tests (c,d). Load vs. deflection curves obtained from the 3-point bending test (e); and stress-strain plots of the tensile test (f).

and bronze matrix of sintered CCFR-bronze and depicted in Fig. 4d. Oxygen and carbon in the structure are inevitable because both elements are released from the binder when they burn out during the debinding process. According to the elemental analysis, the carbon content at the bonding area (point 4) is higher than that in the bronze matrix (point 1).

The dimensions of the printed bending and tensile specimens are $32.4 \times 13.9 \times 6.2 \pm 0.5$ mm and $81.0 \times 9.0 \times 4.1 \pm 0.5$ mm, respectively. Following the debinding process, these dimensions are altered to $31.2 \times 13.3 \times 6.0 \pm 0.5$ mm and $78.1 \times 8.5 \times 4.0 \pm 0.5$ mm. The printed (green), debound (brown) and sintered densities are measured to compare the densification rate in bronze and CCFR-bronze specimens. Table 2 gives the density values and dimensional changes after sintering in three directions. That indicates that bronze has a significantly higher densification rate and shrinkage level than CCFR-bronze. The massive gaps between bronze particles formed by CCF strands (shown in Fig. 4a) prevent the expected densification. These gaps are likely due to the lower measured sintered density in the CCFR-bronze. Besides, the printed CCF in a grid-like structure tends to keep its shape and resists more shrinkage.

Moreover, in both specimens, the shrinkage in the z-direction is slightly higher than that in the other coordinates, probably caused by a more appropriate rearrangement of bronze particles after debinding

due to gravitational force. The average values of electrical conductivity and porosity level, accompanied by their respective standard deviations (SD), measured before and after sintering at room temperature, are displayed in Fig. 5. Analysis demonstrates that the conductivity of CCFR-bronze displays no notable difference before and after sintering owing to the similarity in porosity levels (low level of densification parameter). Further examination of the sintered specimens indicates a decrease in electrical conductivity from 2.351 kS/cm in bronze to 1.46 kS/cm in CCFR-bronze when porosity increases from 27.46 % to 49.53 %. The presence of gaps in the CCFR-bronze structure leads to the reduction in electrical conductivity. Nonetheless, there is no significant decrease in the conductivity of CCFR-bronze compared to bronze, indicating the effectiveness of the CCF material in maintaining conductivity despite increased porosity levels.

Fig. 6 illustrates the visual representation of the bronze and CCFR-bronze specimens, both before and after 3-point bending and tensile tests. Additionally, it presents the corresponding curves derived from these tests. Although each test was performed 3 times, to avoid overcrowding, only one curve is depicted in the graph, as the three curves in each case demonstrated substantial similarity. The bending test results (Fig. 6e) show that flexural strength decreased from 70.08 MPa in bronze to 53.80 MPa in CCFR-bronze (23 % reduction). However,

Table 3
Comparison of mechanical properties (the average values and standard deviation) of Bronze and CCFR-Bronze.

Mechanical properties	Bronze	CCFR-Bronze	Difference, %	Composites in literature [Ref]
Flexural strength (MPa)	70.08 ± 1.28	53.80 ± 0.85	-23.2	107 [66]
Rupture deflection (mm)	2.48 ± 0.09	7.70 ± 0.22	210.5	-
Yield stress (MPa)	36.88 ± 0.49	65.06 ± 0.63	76.4	-
Ultimate tensile strength (MPa)	153.62 ± 2.18	184.31 ± 2.65	19.9	180 [67]
Fracture strain	0.26 ± 0.02	0.34 ± 0.03	30.7	0.27 [67]
Tensile modulus (GPa)	4.66 ± 0.11	13.45 ± 0.28	188.6	-
Theoretical predicted modulus (GPa)	-	13.38	0.5	-

contrasting with the results in this study, Heidari et al. [31] demonstrated an improvement in the bending strength of CCF-reinforced PLA specimens. This variation might be caused by the massive gaps formed during sintering due to adding CCF to bronze. However, the rupture deflection in CCFR-bronze increased by 210 % and reached 7.70 mm. It proves that CCF has considerably enhanced the bronze rupture deflection thrice. Moreover, there is a slight increase in bending load after matrix (bronze) rupture, possibly due to the presence of coherent joints between CCF strands and bronze particles. However, these joints fail after a small amount of deflection (0.6 mm) and lose the strengthening effect, where the CCFR-bronze is crushed.

The stress-strain curves obtained from experimental analysis, as illustrated in Fig. 6f, reveal an improvement in both yield stress and ultimate tensile strength (UTS) of the CCFR-bronze. The yield stress, which is determined by the software interacted with MTS insight machine, exhibits a remarkable increase of 76 %, reaching 65 MPa, when compared to the bronze, while the UTS values improved from 153 MPa to 184 MPa. Additionally, CCF has significantly extended the fracture strain in the CCFR-bronze by 30 %, increasing it from 0.26 to 0.34. Although the measured porosity level of the CCFR-bronze is high (~50 %), leading to expected poor mechanical properties, the results demonstrate remarkable improvements in ductility and toughness compared to the pure bronze with lower porosity (~27.5 %). This improvement could be attributed to the parallel orientation of CCF with the direction of applied force and the acceptable interfacial bonding between CCF and matrix phases. Further analysis of the data demonstrates that Young's modulus of the CCFR-bronze has reached 13.45 GPa, far surpassing that of the bronze, which is recorded at 4.66 GPa. To verify the accuracy of the tensile test results, the Young's modulus of the composite is calculated using the following formula:

$$E_C = E_R V_R + E_M V_M \quad (3)$$

where the volume fractions of reinforcement (V_R) and matrix (V_M) are determined to be 0.06 and 0.94, respectively. Additionally, the Young's modulus of the bronze (porous) specimen (E_M) measured from the tensile test was 4.66 GPa, while the value provided by the manufacturer (150 GPa) was used for E_R . The calculated value of the modulus is found to be 13.38 GPa. This finding provides evidence of a good agreement between the experimental observations and the theoretical predictions. Table 3 presents a summary of the critical mechanical properties of both Bronze and CCFR-Bronze, along with a comparison to composites fabricated using conventional methods.

4. Conclusions

This study has assessed the feasibility of producing a CCFR-bronze

matrix composite using an affordable MEX technique and presented a comprehensive analysis of the material's microstructure and mechanical properties. The elemental and microstructural analyses in this work confirm the successful production of the CCFR-bronze specimen. Microstructure analysis revealed the presence of massive gaps formed by CCF that prevented the expected densification of the composite's structure. However, coherent joints were observed between CCF and bronze particles at the interface areas. Additionally, the electrical conductivity of CCFR-bronze remains relatively high (14.6 kS/cm), demonstrating the low negative impact of CCF material on the conductivity of the composite, despite increased porosity levels (~50 %). The mechanical evaluation of the CCFR-bronze showed a reduction of flexural strength by 23 % due to the formed gaps. Nevertheless, the improved rupture deflection by 210 % and the enhanced yield stress by 76 % demonstrate the effectiveness of incorporating CCF into a bronze matrix. The tensile tests also revealed significant improvements in the composite material's ultimate tensile strength, Young's modulus, and fracture strain. These findings highlight the potential of CCFR-bronze composites produced by the affordable MEX technique in various industrial applications due to their complex geometries and improved mechanical properties. Further studies can be conducted to address the issue of forming gaps between CCF and the matrix. This could involve adding some additives to the raw materials to form liquid phase during sintering process and fill the gaps, and ultimately enhance the mechanical properties.

CRedit authorship contribution statement

Mehrdad Mousapour: Writing – original draft, Methodology, Investigation, Formal analysis. **S Siddharth Kumar:** Writing – original draft, Software, Investigation. **Jouni Partanen:** Writing – review & editing, Investigation, Data curation. **Mika Salmi:** Writing – review & editing, Validation, Supervision, Project administration, Methodology, Data curation.

Declaration of competing interest

The authors declare that they have no known competing financial interests or personal relationships that could have appeared to influence the work reported in this paper.

Acknowledgments

The funding has been received from Jane ja Aatos Erkon Säätiö.

Data availability

The authors are unable or have chosen not to specify which data has been used.

References

- [1] Chung DDL. Processing-structure-property relationships of continuous carbon fiber polymer-matrix composites. *Mater Sci Eng R Rep* 2017;113:1–29.
- [2] Yao SS, Jin FL, Rhee KY, Hui D, Park SJ. Recent advances in carbon-fiber-reinforced thermoplastic composites: a review. *Compos B Eng* 2018;142:241–50.
- [3] Das TK, Ghosh P, Das NC. Preparation, development, outcomes, and application versatility of carbon fiber-based polymer composites: a review. *Adv Compos Hybrid Mater* 2019;2:214–33.
- [4] Zheng H, Zhang W, Li B, Zhu J, Wang C, Song G, Wu G, Yang X, Huang Y, Ma L. Recent advances of interphases in carbon fiber-reinforced polymer composites: a review. *Compos B Eng* 2022;233:109639.
- [5] Chung D. Carbon fiber composites. Elsevier; 2012.
- [6] Cogswell FN. Thermoplastic aromatic polymer composites: a study of the structure, processing and properties of carbon fiber reinforced polyetheretherketone and related materials. Elsevier; 2013.
- [7] Morgan P. Carbon fibers and their composites. CRC press; 2005.
- [8] Botelho EC, Silva RA, Pardini LC, Rezende MC. A review on the development and properties of continuous fiber/epoxy/aluminum hybrid composites for aircraft structures. *Mater Res* 2006;9:247–56.

- [9] Ishikawa T, Amaoka K, Masubuchi Y, Yamamoto T, Yamanaka A, Arai M, Takahashi J. Overview of automotive structural composites technology developments in Japan. *Compos Sci Technol* 2018;155:221–46.
- [10] Kroll L, Meyer M, Nendel W, Schormair M. Highly rigid assembled composite structures with continuous fiber-reinforced thermoplastics for automotive applications. *Procedia Manuf* 2019;33:224–31.
- [11] Salgado R, Lopes C, Szojda L, Araújo P, Gorski M, Velez FJ, Castro-Gomes J, Krzywon R. Carbon fiber epoxy composites for both strengthening and health monitoring of structures. *Sensors* 2015;15(5):10753–70.
- [12] Olofin I, Liu R. The application of carbon fiber reinforced polymer (CFRP) cables in civil engineering structures. *Int J Civ Eng* 2015;2(7):1–5.
- [13] Davies-Frey D, Bowkett M, Constant E, Thanapalan K. Failure detection of composite materials in sport applications. In: 7th International conference on control, decision and information technologies (CoDIT). IEEE, June; 2020. p. 563–7.
- [14] Zhang J, Lin G, Vaidya U, Wang H. Past, present and future prospective of global carbon fibre composite developments and applications. *Compos B Eng* 2023;250:110463.
- [15] Akmal JS, Salmi M, Hemming B, Teir L, Suomalainen A, Kortensniemi M, Partanen J, Lassila A. Cumulative inaccuracies in implementation of additive manufacturing through medical imaging, 3D thresholding, and 3D modeling: a case study for an end-use implant. *Appl. sci* 2020;10(8):2968.
- [16] Kretschmar N, Chekurov S, Salmi M, Tuomi J. Evaluating the readiness level of additively manufactured digital spare parts: an industrial perspective. *Appl. sci* 2018;8(10):1837.
- [17] Mousapour M, Partanen J, Salmi M. NiTiCu alloy from elemental and alloyed powders using vat photopolymerization additive manufacturing. *Addit Manuf* 2023;78:103853.
- [18] Chekurov S, Metsä-Kortelainen S, Salmi M, Roda I, Jussila A. The perceived value of additively manufactured digital spare parts in industry: an empirical investigation. *Int J Prod Econ* 2018;205:87–97.
- [19] Salmi M, Tuarte IF, Chekurov S, Huotilainen E. Effect of build orientation in 3D printing production for material extrusion, material jetting, binder jetting, sheet object lamination, vat photopolymerisation, and powder bed fusion. *Int J Collab Enterp* 2016;5(3–4):218–31.
- [20] Mousapour M, Salmi M, Klemettinen L, Partanen J. Feasibility study of producing multi-metal parts by Fused Filament Fabrication (FFF) technique. *J Manuf Process* 2021;67:438–46.
- [21] Kabir SF, Mathur K, Seyam AFM. A critical review on 3D printed continuous fiber-reinforced composites: history, mechanism, materials and properties. *Compos Struct* 2020;232:111476.
- [22] Van de Werken N, Tekinalp H, Khanbolouki P, Ozcan S, Williams A, Tehrani M. Additively manufactured carbon fiber-reinforced composites: state of the art and perspective. *Addit Manuf* 2020;31:100962.
- [23] Struzziero G, Barbezat M, Skordos AA. Consolidation of continuous fiber reinforced composites in additive processes: a review. *Addit Manuf* 2021;48:102458.
- [24] Qu P, Kong H, Li X, Lei Y, Guo A, Wang S, Wang H, Hu Y, Wan Y, Takahashi J. Additive manufacturing of hybrid continuous carbon/basal fiber reinforced composites based on bi-matrix co-extrusion. *JMR&T* 2024;30:8683–704.
- [25] Cheng P, Peng Y, Li S, Rao Y, Le Duigou A, Wang K, Ahzi S. 3D printed continuous fiber reinforced composite lightweight structures: a review and outlook. *Compos B Eng* 2023;250:110450.
- [26] Liu G, Xiong Y, Zhou L. Additive manufacturing of continuous fiber reinforced polymer composites: design opportunities and novel applications. *Compos Commun* 2021;27:100907.
- [27] Zhuo P, Li S, Ashcroft IA, Jones AI. Material extrusion additive manufacturing of continuous fiber reinforced polymer matrix composites: a review and outlook. *Compos B Eng* 2021;224:109143.
- [28] Zhang H, Huang T, Jiang Q, He L, Bismarck A, Hu Q. Recent progress of 3D printed continuous fiber reinforced polymer composites based on fused deposition modeling: a review. *J Mater Sci* 2021;56(23):12999–3022.
- [29] Yu T, Zhang Z, Song S, Bai Y, Wu D. Tensile and flexural behaviors of additively manufactured continuous carbon fiber-reinforced polymer composites. *Compos Struct* 2019;225:111147.
- [30] Naranjo-Lozada J, Ahuett-Garza H, Orta-Castañón P, Verbeeten WM, Sáiz-González D. Tensile properties and failure behavior of chopped and continuous carbon fiber composites produced by additive manufacturing. *Addit Manuf* 2019;26:227–41.
- [31] Heidari-Rarani M, Rafiee-Afarani M, Zahedi AM. Mechanical characterization of FDM 3D printing of continuous carbon fiber reinforced PLA composites. *Compos B Eng* 2019;175:107147.
- [32] Lu Y, Han X, Gleadall A, Chen F, Zhu W, Zhao L. Continuous fibre reinforced Vat photopolymerisation (CONFIB-VAT). *Addit Manuf* 2022;60:103233.
- [33] Kumar SS, Akmal JS, Salmi M. 4D printing of shape memory polymer with continuous carbon fiber. *Prog. Addit. Manuf* 2023:1–11.
- [34] Akmal J, Salmi M. Additive manufacturing of self-sensing parts through material extrusion. *Virtual Phys Prototyp* 2024;19(1):e2321200.
- [35] Li X, Qu P, Kong H, Zhu Y, Hua C, Guo A, Wang S. Multi-scale numerical analysis of damage modes in 3D stitched composites. *Int J Mech Sci* 2024;266:108983.
- [36] Shirvanimoghaddam K, Hamim SU, Akbari MK, Fakhrooseini SM, Khayyam H, Paksresht AH, Ghasali E, Zabet M, Khrram Shahzad Munir, Shian J, Davim JP, Naebe M. Carbon fiber reinforced metal matrix composites: fabrication processes and properties. *Compos. A: Appl. Sci. Manuf* 2017;92:70–96.
- [37] Mahaviradhan N, Sivaganesan S, Sravya NP, Parthiban A. Experimental investigation on mechanical properties of carbon fiber reinforced aluminum metal matrix composite. *Mater Today Proc* 2021;39:743–7.
- [38] Miranda AT, Bolzoni L, Barezar N, Huang Y, Shin J, Ko SH, McKay BJ. Processing, structure and thermal conductivity correlation in carbon fibre reinforced aluminium metal matrix composites. *Mater Des* 2018;156:329–39.
- [39] Silvain JF, Veillère A, Lu Y. Copper-carbon and aluminum-carbon composites fabricated by powder metallurgy processes. *J. Phys* 2014;525(1):012015.
- [40] Mu W, Lin J, Liu E, Zhou C, He W. Fabrication of continuous carbon-fibers reinforced aluminum matrix composites and coating evolution during heat treatment. *JMR&T* 2022;17:1852–67.
- [41] Jacquesson M, Girard A, Vidal-Sétif MH, Valle R. Tensile and fatigue behavior of Al-based metal matrix composites reinforced with continuous carbon or alumina fibers: Part I. Quasi-unidirectional composites. *METALL MATER TRANS A* 2004;35:3289–305.
- [42] Hou LG, Wu RZ, Wang XD, Zhang JH, Zhang ML, Dong AP, Sun BD. Microstructure, mechanical properties and thermal conductivity of the short carbon fiber reinforced magnesium matrix composites. *J Alloys Compd* 2017;695:2820–6.
- [43] Wan YZ, Wang YL, Luo HL, Dong XH, Cheng GX. Effects of fiber volume fraction, hot pressing parameters and alloying elements on tensile strength of carbon fiber reinforced copper matrix composite prepared by continuous three-step electrodeposition. *Mater. Sci. Eng. A* 2000;288(1):26–33.
- [44] Liu L, Tang Y, Zhao H, Zhu J, Hu W. Fabrication and properties of short carbon fibers reinforced copper matrix composites. *J Mater Sci* 2008;43:974–9.
- [45] Tang Y, Liu H, Zhao H, Liu L, Wu Y. Friction and wear properties of copper matrix composites reinforced with short carbon fibers. *Mater Des* 2008;29(1):257–61.
- [46] Ali S, Ahmad F, Shirazi MI, Malik K, Raza MR, Memon IR. Flow-induced fiber orientation in short carbon fiber reinforced copper matrix composites. *Mater Today Commun* 2022;33:104855.
- [47] Even C, Arvieu C, Quenisset JM. Powder route processing of carbon fibres reinforced titanium matrix composites. *Compos Sci Technol* 2008;68(6):1273–81.
- [48] Kondoh K. Titanium metal matrix composites by powder metallurgy (PM) routes. In: *Titanium powder metallurgy*. Butterworth-Heinemann; 2015. p. 277–97.
- [49] Jiao F, Liu M, Jiang F, Zhao J, Li P, Wang Z. Continuous carbon fiber reinforced Ti/Al3Ti metal-intermetallic laminate (MIL) composites fabricated using ultrasonic consolidation assisted hot pressing sintering. *Mater. Sci. Eng. A* 2019;765:138255.
- [50] Zeng C, Zhang B, Eftefagh AH, Wen H, Yao H, Meng WJ, Guo S. Mechanical, thermal, and corrosion properties of Cu-10Sn alloy prepared by laser-powder-bed-fusion additive manufacturing. *Addit Manuf* 2020;35:101411.
- [51] Karthik M, Abhinav J, Shankar KV. Morphological and mechanical behaviour of Cu-Sn alloys—a review. *Met. Mater. Int* 2021;27:1915–46.
- [52] Mehta A, Zhou L, Hyer H, Huynh T, Lu B, Graydon K, Drobner EJ, Park SH, Sohn Y. Microstructural characteristics and mechanical properties of additively manufactured Cu-10Sn alloys by laser powder bed fusion. *Mater. Sci. Eng. A* 2022;838:142775.
- [53] Yang P, He D, Shao W, Tan Z, Guo X, Lu S, Anton K. Study of the microstructure and mechanical properties of Cu-Sn alloys formed by selective laser melting with different Sn contents. *J Mater Res Technol* 2023;24:5476–85.
- [54] Güngör K, Demirer A. Investigation of dry sliding friction wear behavior of CuSn11 bronze plain bearing applying impregnated graphite-filled PTFE. *Tribol. T* 2022;65(5):880–91.
- [55] Zhao L, Li J, Yang Q, Wang Y, Zhang X, Li H, Yang Z, Xu D, Liu J. Study on friction and wear properties of new self-lubricating bearing materials. *Crystals* 2022;12(6):834.
- [56] Chen S, An D, Bi Y, Liang J, Liu C. Preparation of novel polytetrafluoroethylene/copper-matrix self-lubricating composite materials. *J Compos Mater* 2014;48(13):1561–74.
- [57] Lu Z, Ayeni OI, Yang X, Park HY, Jung YG, Zhang J. Microstructure and phase analysis of 3D-printed components using bronze metal filament. *JMEP* 2020;29:1650–6.
- [58] Kılınc AÇ, Goktas AA, Keskin ÖY, Köktaş S. Extrusion-based 3D printing of CuSn10 bronze parts: production and characterization. *Metals* 2021;11(11):1774.
- [59] Azarov AV, Antonov FK, Vasil'Ev VV, Golubev MV, Krasovskii DS, Razin AF, Salov VA, Stupnikov VV, Khaziev AR. Development of a two-matrix composite material fabricated by 3D printing. *Polym Sci D* 2017;10:87–90.
- [60] Adumitroaie A, Antonov F, Khaziev A, Azarov A, Golubev M, Vasiliev VV. Novel continuous fiber bi-matrix composite 3-D printing technology. *Materials* 2019;12(18):3011.
- [61] German RM. *Liquid phase sintering*. New York, NY: Springer; 1985.
- [62] Mousapour M, Azadbeh M, Danninger H. Effect of compacting pressure on shape retention during supersolidus liquid phase sintering of Cu base alloys. *Powder Metall* 2017;60(5):393–403.
- [63] Mousapour M, Azadbeh M, Danninger H. Feasibility study of 'elephant foot' phenomenon during liquid phase sintering of systems with volatile components. *Powder Metall* 2016;59(5):321–8.
- [64] Ghasemi S, Azadbeh M, Mousapour M, Mohammadzadeh A, Danninger H, Salimi N. The role of pore evolution during supersolidus liquid phase sintering of prealloyed brass powder. *Powder Metall* 2020;63(2):187–96.
- [65] Mousapour M, Azadbeh M, Mohammadzadeh A, Danninger H. On the deflection behaviour of prealloyed alpha brass during sintering: in-situ bending technique and modelling. *Powder Metall* 2020;63(2):134–41.
- [66] Xia L, Jia B, Zeng J, Xu J. Wear and mechanical properties of carbon fiber reinforced copper alloy composites. *Mater. Charact* 2009;60(5):363–9.
- [67] Jun Z. Tensile and friction properties of tin bronze matrix composites reinforced by carbon fibers. *Tribol Lett* 2010;40(3):311–7.